

Bedrock architecture, soil texture, and hyporheic zone characterization combining electrical resistivity and induced polarization imaging

Dale F. Rucker^{a,*}, Chia-Hsing Tsai^b, Kenneth C. Carroll^b, Scott Brooks^c, Eric M. Pierce^c, April Ulery^b, Christopher Derolph^c

^a hydroGEOPHYSICS, Inc., Tucson, AZ, USA

^b Plant & Environmental Sciences Department, New Mexico State University, Las Cruces, NM, USA

^c Oak Ridge National Laboratory, Environmental Sciences Division, Oak Ridge, TN, USA

ARTICLE INFO

Article history:

Received 4 May 2020

Received in revised form 24 November 2020

Accepted 6 March 2021

Available online 09 March 2021

Keywords:

Bedrock mapping

Soil texture

Chargeability

Resistivity

Hyporheic zone

ABSTRACT

The shallow (<15 m depth) subsurface environment of a short reach along a bedrock stream was investigated with electrical resistivity and induced polarization (IP) to map details of bedrock and soil sediments. The bedrock is mostly comprised of limestone, and is generally resistive compared to the overlying soil. The soil-bedrock interface was determined through a trial and error approach using a sharp boundary feature in the inversion model. The inferred bedrock surface determined from the inversions exhibited undulating patterns with troughs and ridges. A near continuous trough ran alongside the stream within the floodplain, and is suggestive of a paleochannel among other interpretations of this feature. The structure of the electrical resistivity above the bedrock showed small-scale elongated features. The chargeability from the IP method showed larger scale features. High values of chargeability were associated with the sediments in the floodplain, and low values were associated with bedrock, stream, and soil on the elevated banks above the stream. If the chargeability is associated with membrane polarization characteristic of clayey soils, then IP seems to highlight the mere existence of clay, while the resistivity may be more discernable of the relative proportion of clay. Vegetation differences may also explain the chargeability distribution, where parts of the survey with high chargeability had dense pine with no understorey making the soils more organically rich.

© 2021 Elsevier B.V. All rights reserved.

1. Introduction

Both exposed and buried lithofacies within hyporheic zones are a significant controlling factor for mass transfer of nutrients and pollutants at the groundwater-surface water interface. The hyporheic zone acts as the bridge that links these two systems by active fluid mixing and exchange (Anibas et al., 2016), ultimately serving as the regulator of riverine ecosystems (Crook et al., 2008). Exchange through the hyporheic zone spans a wide range of spatial scales, and is influenced by stream morphology and heterogeneity (Boano et al., 2014; Pryshlak et al., 2015). As poignantly indicated by Ward et al. (2014), relatively little is known about the distribution of hyporheic transport processes in the subsurface. Even more recently, Clémence et al. (2017) propounded that ‘despite many improvements in both general and regional-scale studies, there is a lack of information of the local scale and of precise descriptions of the mixture and movement of water within riverbed sediments’. As evident by a large body of work, characterizing the hyporheic zone is an ongoing, major, and multidisciplinary

focus of study for many (e.g., Magliozzi et al., 2019; Ren et al., 2019; Sherman et al., 2019; and the references contained therein).

Direct characterization of hyporheic sediments greater than a meter or so is difficult due to access by heavy duty rigs needed to push or drill for soil samples (Crook et al., 2008) and by scale limitations of the samples collected. On the other hand, many non-invasive geophysical studies have been conducted for hyporheic zone characterization. In fact, geophysical methods often overcome the access limits based on lighter equipment requirements and the ability to image deeply into the earth from surface-only based measurements (Rucker, 2010). These studies mainly focus on mapping the electrical properties of the subsurface using ground penetrating radar (GPR) (e.g., Bianchin et al., 2011; Mermillod-Blondin et al., 2015) and electromagnetics (Steelman et al., 2017; Gaona et al., 2019). The focus on electrical and electromagnetic methods mainly stem from the fact that many hydrogeological parameters important for hyporheic zone studies such as water content, tortuosity, porosity, and granular surface area can be related to electrical conductivity, permittivity, and chargeability. A less popular side of geophysical methods for hydrogeology, seismic methods, have also been applied to hyporheic zone studies and more broadly riparian systems (Hsu et al., 2011; Schmandt et al., 2013; Roth et al., 2016) in order to

* Corresponding author.

E-mail address: druck8204@gmail.com (D.F. Rucker).

help with understanding porosity and stratigraphy (McLachlan et al., 2017).

By far, the most popular geophysical method for hyporheic studies is the electrical resistivity imaging (ERI) or geoelectrical imaging method (e.g., Cardenas and Markowski, 2010; Ward et al., 2010; Toran et al., 2013). Miller et al. (2014) used ERI to image a gravel-dominated flood plain and fines as it related to hydraulic conductivity. Crook et al. (2008) used ERI to map structure and estimate the volume of fluvial deposits along streams. Time lapse ERI is also used to monitor changes in resistivity as they may relate to tracer tests (Ward et al., 2010; Clémence et al., 2017) or river stage (Johnson et al., 2012). A secondary measurement of ERI, induced polarization (IP), has also been used in hyporheic studies to map hydraulic conductivity differences in soils by focusing on the amount and type of finely textured soils, for example the studies by Mwakanyamale et al. (2012) and Benoit et al. (2019). More generally, others have studied the strong link between chargeability from IP and soil properties (e.g., Weller et al., 2015; Nordsiek et al., 2016; Maurya et al., 2018). None of these works, however, specifically used ERI and IP to map bedrock and soil texture of a shallow bedrock stream.

A deeper understanding of the hyporheic zone is necessary to advance our understanding of watershed function. Hyporheic water exchange may play an important role in contaminant fate and transformation through processes such as sorption and desorption, precipitation and dissolution, and oxidation-reduction reactions that alter chemical and toxicological behavior. Therefore, in this work we applied ERI and IP to gain a deeper understanding of the hyporheic zone and surrounding stream bank and flood plain to map bedrock architecture and sediment soil texture along a third-order shallow limestone bedrock stream. The geophysical study is part of a larger effort to define mercury (Hg) flux through the hyporheic zone along a reach of the East Fork Poplar Creek (EFPC) near the Oak Ridge National Laboratory (ORNL) (Brooks and Southworth, 2011). In the case of Hg, the processes of methylation to form the potent neurotoxin monomethyl mercury (MMHg) and demethylation of MMHg to re-generate inorganic Hg[II] (Dong et al., 2010) are significant. Mercury methylation in the environment is mediated by several clades of anaerobic microorganisms under anoxic conditions that occur in some hyporheic environments (Gilmour et al., 2013).

We conducted ERI and IP geophysical surveys at a reconnaissance scale, with 10 transects across a 250 m meandering reach of the EFPC with the objectives of (i) identifying and delineating the unconsolidated soils-bedrock interface, (ii) assessing variations in sediment texture, and (iii) inferring underlying bedrock architecture. A secondary set of analyses were conducted to test the best array to use across the survey area, comparing the dipole-dipole array with a newer Alt3_Wenner array (Cubbage et al., 2017). We also investigated different bedrock picking algorithms. The overall results from all 10 lines show distinct differences in architecture at point bars, straight runs, cut banks, and floodplains. The work contributes to the small and growing body of research characterizing the hyporheic zone with ERI and IP. Additionally, this work is novel in terms of the type of stream, the scale at which the geophysics was applied, the geophysical acquisition methodology, and the unique findings.

1.1. Study area

The EFPC begins at the Y-12 National Security Complex (Y-12 NSC), a US Department of Energy facility in the southern Appalachians of eastern Tennessee, USA (Fig. 1a). It is a perennial stream with flow originating from springs, groundwater, storm water runoff, and process and cooling water from Y-12 NSC operations (Brooks et al., 2017). The creek flows generally westward for approximately 26 km to the confluence of Poplar Creek. Stations along the creek are designated EFKx (which stands for East Fork, x kilometers from the stream mouth); our specific study area was at EFK5.4 which is 5.4 km upstream from the

confluence. In 2016, the stream flow rates at EFK5.4 varied from a late fall base flow of 0.63 m³/s to a winter storm-derived high of 34.5 m³/s. The average for the year was 1.45 m³/s. During the summer of 2017, when the geophysical campaign started, flows were similar. Water conductivity was 438 µS/cm and the temperature was 22C.

Mercury is the primary contaminant of concern along EFPC due to the historic discharges at the headwaters and consequent contamination of creek sediments and floodplain soils (Brooks and Southworth, 2011). Although remedial actions over the past 25 years have significantly decreased overall Hg releases to the environment, low levels of Hg continue to be released, and the surface water, bed sediments, creek banks, and floodplain soils contain high levels of residual Hg as a consequence. Recent detailed sampling and calculations, coupled with stable Hg isotope fractionation patterns, indicate that more than 50% of the Hg load in EFPC originates from diffuse legacy sources of Hg outside of Y-12 NSC, and that interstitial pore water within the hyporheic zone may be an important secondary source of the additional Hg loading to the surface water (Demers et al., 2018; Peterson et al., 2018).

Hydrogeologically, the principal groundwater-containing formations in this area include Knox Dolomite and Chickamauga Limestone (Loar et al., 2011). The substrate in EFPC consists predominately of a mixture of gravels and cobbles, with outcrops of bedrock distributed through the entire length of the stream. Fine-grained deposits line the channel margins. Several studies over the years include some level of sediment characterization, soil bank mapping, and spot drilling within the hyporheic zone (Fig. 1b, c). Detailed soil texture information for samples collected from the surface of the exposed creek bank are provided in Dickson et al. (2015, 2019). Surface sediment samples collected at low spatial density provides some level of confirmation and context of soil texture (Brooks et al., 2017). The few borings that exist have detailed soil data associated with them, and also show where the borings hit bedrock by refusal. The point of refusal could have been a weathered bedrock surface, as it is unknown if the material was competent while still showing refusal. In 2012, the four NHSB series of piezometers were installed with a Geoprobe to refusal (2.8–2.9 m). The soil descriptions for these four geological logs are very consistent among each other with a maximum distance between any pair being 4.8 m. The water level recorded in these piezometers was just above 230 m (above mean sea level, amsl); the elevation of the streambed along Line 2 was measured with a GPS at 229.84 m amsl, suggesting a hydraulic gradient towards the gaining stream. The most recent set of drilling, holes D-1 through D-3, were conducted with a shallow auger rig. Drillhole D-1 was open, meaning that no refusal was met by the 3 m drill. D-3 was the only hole that had a geological description in the driller's log (sands and gravels).

2. Methods

2.1. Geophysical acquisition

The ERI method is conducted by passing electrical current and measuring the resulting electrical field through a series of grounded electrodes evenly spaced along a 2D transect (Loke et al., 2013). A resistivity acquisition system using a computer-based switching system controls which specific electrodes transmit or receive electrical current or voltage (Loke et al., 2020). The acquisition system can be powered by vehicle batteries or a generator, with a transformer that controls how the output current is transmitted. A square wave with on and off times, incorporating polarity reversal, is a popular means of current transmission. In our study, we used the 8-channel SuperSting R8 (Advanced Geosciences, Inc., Austin, TX) with stainless steel electrodes spaced 3 m apart along an 81 m transect. Through the stream, which had widths of 6 to 14 m and upwards of 0.5 m of water, the cable was placed at the bottom of the stream. The specific spatial arrangement of current electrodes relative to voltage measurement electrodes is referred to as an array. The dipole-dipole array is rather popular for

along the EFPC, we expect the chargeability measured with IP to be controlled by clay mineral membrane polarization (Johansson et al., 2015). Since the secondary voltage is very small compared to the primary voltage, an integral measure of the decay curve is calculated to extract the IP signal (Ntarlagiannis et al., 2016). There is an initial delay of 65 milliseconds (ms) within our resistivity meter. To improve the accuracy of the integration, the decay curve was parsed into six windows (or gates) that are linearly distributed across the voltage decay time. For each of the six windows, the equipment provides a partial chargeability value (Florsch et al., 2011) and the final summed apparent chargeability in the raw data file.

An automated inverse methodology, applied through numerical models, was used to convert the measured resistance and apparent chargeability to an estimate of the true resistivity and chargeability. The inverse method relied on nonlinear optimization, requiring an iterative procedure to march towards a solution. Its objective was to minimize the difference between the modeled and measured data, using a weighted least squares algorithm. The objective function has been updated many times over the years to also include other terms, such as smooth model constraints (i.e., a smooth model based on minimizing the second spatial derivative of the resistivity). In our work along the EFPC, inverse modeling was carried out for ERI and IP using RES2DINVx64 (Loke, 2017). For a more detailed discussion of inversion methodology, equations, and assumptions, please refer to Loke et al. (2013).

2.2. Survey design

Given that the array type can greatly influence data quality and resolution, we compared the dipole-dipole array and Alt3_Wenner array (Cubbage et al., 2017) along Line 4 (Fig. 1b) to determine which was best for data acquisition across the entire field study. The dipole-dipole array has its voltage measurement electrode pairs external to the current electrode pairs. It is the array of highest overall resolution (Loke et al., 2010), but with the lowest signal-to-noise. Historically, it has been a popular array to use for hyperheic studies. The Alt3_Wenner array was created as an alternative to the Wenner array, an array that can only use one channel, by filling the remaining unused channels of a multi-channel acquisition system with gradient array measurements. The spatial resolution of the Wenner array is not as good as the dipole-dipole array in the near surface, however its signal to noise is far superior and data are less noisy at depth. The resolution of the Wenner array is greatly enhanced with the addition of the gradient array and the total number of resistance measurements exceeds that of the dipole-dipole array.

Both arrays were tested with 28 electrodes, creating 216 data records for the dipole-dipole array in 96 min and 543 data records for the Alt3_Wenner in 55 min (Table 1). Both arrays have similar measured apparent resistivity and chargeability values. However, a statistic that stands out for representing data quality is the 'Percentage of decay curves with a negative value', where a negative value occurs in at least one of the six integrated windows of the decay curve. This is one of the parameters used to help filter noisy data from eventual inverse modeling. Here, the Alt3_Wenner has a significantly lower number than dipole-dipole. Seeing that the dipole-dipole array is starting from a lower number of total measurements, the higher noise from IP

measurements significantly reduces its data contribution to inverse modeling.

The data for the two arrays were inverted using the robust model constraint, based on the L1 norm, and higher dampening for the first layer, which are common settings within RES2DINVx64. The grid structure for each array was based on the finite element method, with the dipole-dipole array having 351 cells and the Alt3_Wenner having 1026 cells. The larger number of cells for modeling of Alt3_Wenner data was justified by the larger number of measurements. The inversion model results, displayed in Fig. 2, show very similar outcomes between the two arrays, but with subtle differences. First, both sets of results show the resistivity generally transitioning from near surface conductive material to deeper resistive material (Fig. 2a and d). The chargeability also shows segregated higher values in the near surface at the beginning of the line and very low values in the stream with exposed bedrock (from about 42 to 55 m along the line), as shown in Fig. 2b and e. The normalized chargeability (Fig. 2c and f), where chargeability is divided by the resistivity on a cell-by-cell basis, is also very similar in overall character. The main difference in the resistivity is the split in the resistive material for the dipole-dipole array at around 37 m. In addition, the edges of the high resistivity layer appear to dive deep for dipole-dipole likely due to lower resolution for this array on the edges. The chargeability data for the dipole-dipole array shows a moderate vertical feature at around 55 to 60 m, which is not present in the Alt3_Wenner array.

Based on data quality, quantity, and modeling results (including the root mean square (RMS) error between measured and modeled resistance data), we collected the remaining nine geophysical lines with the Alt3_Wenner array (Fig. 1b). While the original work on this array from Cubbage et al. (2017) only focused on resistivity, we believe it is perfectly suited for chargeability as well based on the low noise statistics presented in Table 1. The decay curves were less noisy with fewer decay curves comprising a negative value and are more numerous overall. Lastly, the array enhances visualization of the subsurface at the edges of the line. Normally, due to low model resolution and data sensitivity in the lower corners, the model results are cut in a triangular shape. The dipole-dipole results confirm the low sensitivity with vertical contours in the lower corners. The horizontal contouring for the Alt3_Wenner demonstrates the sensitivity of the array remains relatively high with depth.

2.3. Interface picking

It is fairly common to use automated routines to find interfaces in resistivity data (e.g., Nguyen et al., 2005; Hsu et al., 2010). For bedrock systems, Chambers et al. (2013, 2014) have demonstrated a number of methods that include calculating the second derivative along the z axis of modeled data (called the steepest gradient method, or SGM), picking a known reasonable resistivity value that would represent the top of the bedrock (referred to as the known interface method, or KIM), and a c-means clustering method (or CLS). An example of KIM is shown in the resistivity profiles of Fig. 3, where a value near 500 Ω -m (or log transformed resistivity value of 2.7) has a thick solid black line to estimate the transition that likely results from unconsolidated sediment changing to bedrock.

Table 1
Data statistics for the array comparison along the EFPC, acquisition Line 4.

Array	Number of measurements	Acquisition time (min)	Avg. apparent resistivity (ohm-m)	Avg. apparent chargeability (ms)	Percent of decay curves with a negative value	RMS ^a error at iteration 5
Dipole-Dipole	216	96	287	4.47	19	3.5
Alt3_Wenner	543	55	285	5.69	7	1.2

^a RMS = root mean square.

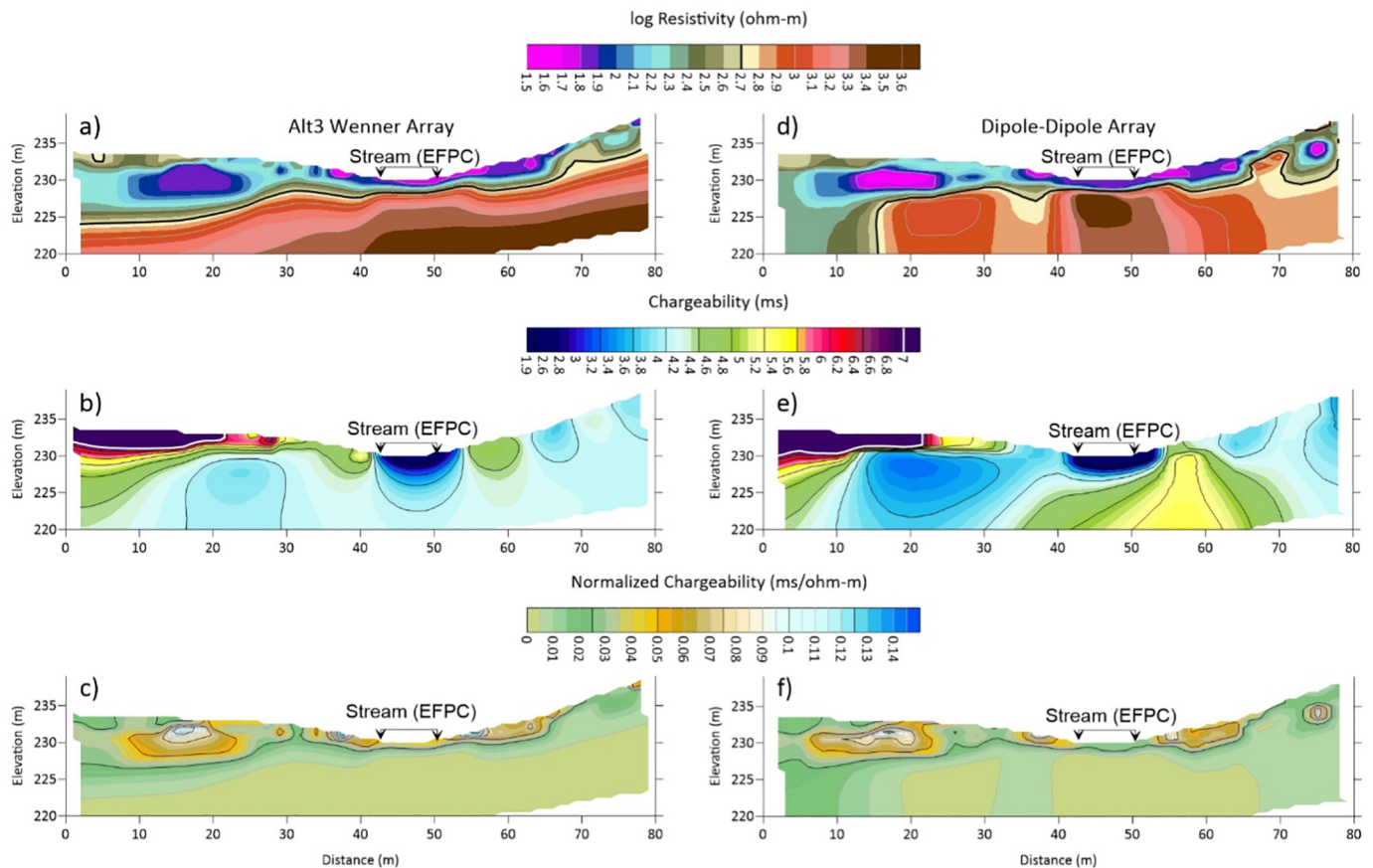


Fig. 2. Array comparison between the Alt3_Wenner and dipole-dipole arrays along Line 4, with cross section looking down stream: a) ERI inversion results for the Alt3_Wenner array; b) IP inversion results for the Alt3_Wenner array; c) normalized chargeability for the Alt3_Wenner array; d) ERI inversion results for the dipole-dipole array; e) IP inversion results for the dipole-dipole array; f) normalized chargeability for the dipole-dipole array.

Elwaseif and Slater (2012) used a first derivative filter on resistivity models called the Roberts' cross-gradient operator (Roberts, 1963). They further used the edge detection in a two-step inversion by incorporating it as an initial guess and conducting a 'disconnect' inversion with the location of the interface updated iteratively. The disconnected boundary removes the smoothness constraint across the layers to allow for sharp transition in resistivity values above and below the interface. In RES2DINVx64, this boundary is referred to as a sharp boundary and can be assigned a fixed value for cells above or below the boundary, or left open for the inversion process to calculate the resistivity above and below the boundary.

For the resistivity data collected along EFPC using the Alt3_Wenner array, we compared the Roberts' filter of Elwaseif and Slater (2012) and KIM interface methods. The KIM was applied by assuming the sharp boundary coincided with log resistivity values of 2.4, 2.7, and 3.0 (Fig. 3a). The location of each threshold is shown across the profile as a different line style. The sharp boundary inversion was conducted using identical parameters as the no sharp boundary model (Fig. 3a), but with a sharp boundary that assumed no values either above or below it. Using the KIM, the model with the lowest RMS error was that with a boundary at 2.7 (Fig. 3c). The fitted resistivity values for the high resistivity material are uniform across the space compared to the other models which show a larger variability in basement resistivity values (Fig. 3b and d).

A Robert's filter, as implemented through the software Surfer (Golden Software), was applied to the no boundary model (Fig. 3e). Values for filtered data ranged from about -300 to over $400 \Omega\text{-m/m}$. Interface threshold values of 30, 90, and 150 were chosen for comparison. The location of each threshold is shown across the profile as a different line style. When the contour for a particular threshold

value was not continuous across the profile or if more than one contour was present along any lateral position, we used expert judgment to pick the best interface location. The interface for the Roberts' filter was similar to KIM, but subtle differences can be seen.

The model with a threshold of $90 \Omega\text{-m/m}$ has the lowest RMS and a lower variability in basement resistivity (Fig. 3g) compared to the other two models (Fig. 3f, h). The RMS is on par with the no boundary option and with KIM using a threshold of 2.7. However, the variability below the interface is higher with the Roberts' filter method as it appears to have fit lower values than the overall mean value towards the end of the line. For this reason, the KIM was used to process all the lines.

3. Results

3.1. Inversion of remaining lines

Having selected the Alt3_Wenner array and KIM methods for data acquisition and processing, all ten lines along the EFPC underwent the same processing procedure for inversion and iterative interface picking to model both electrical resistivity and chargeability from the IP method. The interface is shown as a heavy black line that separates the upper conductive material and lower resistive material. Fig. 4 shows the results for the first five lines, which were acquired along the straight run of EFPC. Line 5, which is closest to the stream curve and a large cut bank on the north side, is approximately nine stream-widths downgradient of the curve. A floodplain exists on the southern portion of each line and a steep bank is on the north. Lines 1 and 2 were placed near a small unnamed ephemeral tributary to EFPC. The chargeability from IP models all show very low to moderately low values that generally range from 2 to 4 ms. Notice Line 5 is missing an

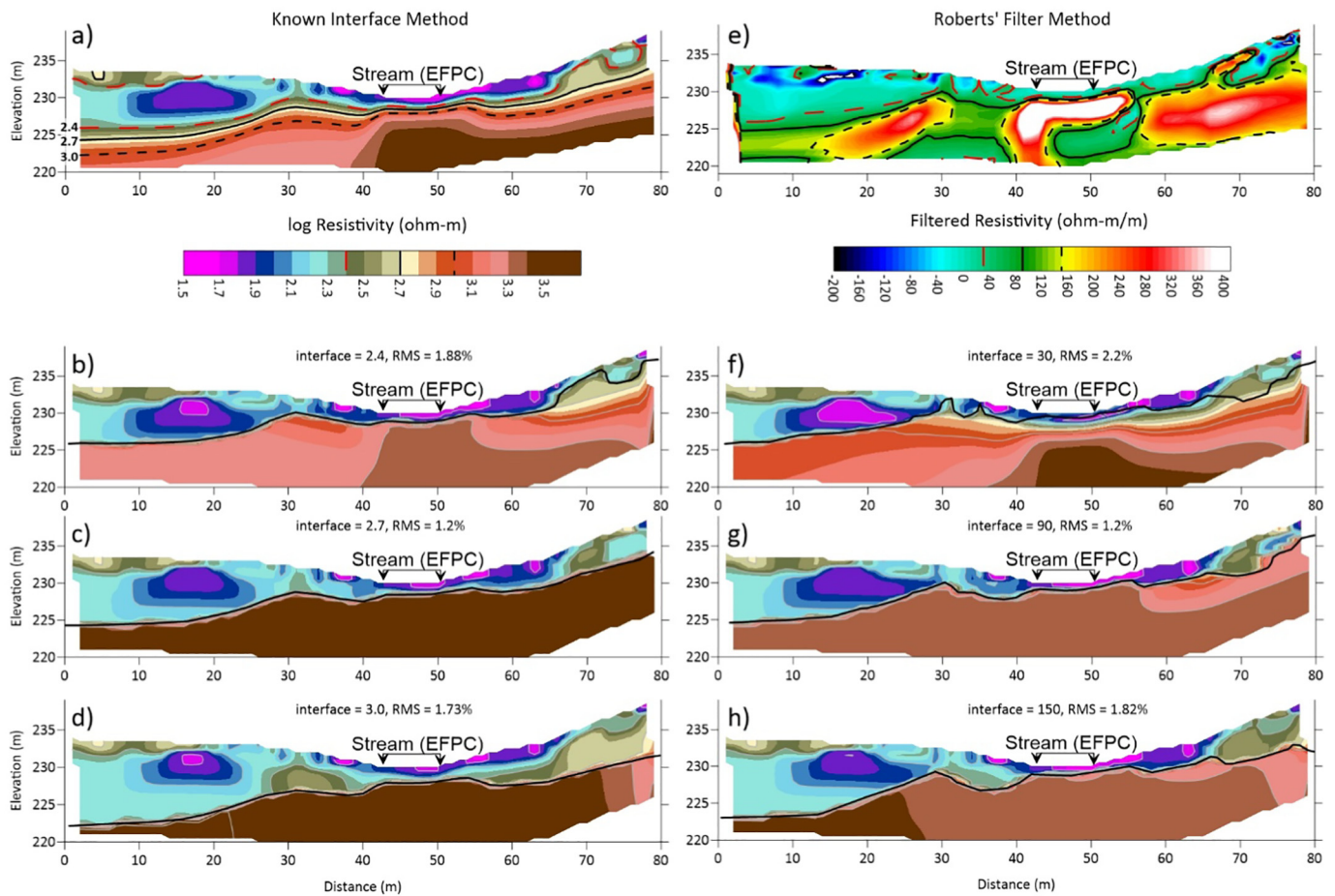


Fig. 3. Interface picking for Line 4 resistivity data collected by Alt3_Wenner array and using KIM (a, b, c, d); or Roberts' filter method (e, f, g, h). Three threshold values were used in each method for picking the interface and tested for model error and resistivity variability.

IP model, because excessive noise in the data prevented reliable model generation.

Similar to Lines 1 through 5, in Lines 6 through 10 the resistivity has a fairly narrow range of values below the interface (Fig. 5). The exception is Line 7, which shows a strong vertical conductive feature at the base of a headcut starting at about 50 m. The IP data for the bedrock shows fairly low chargeability values with the exception of Line 9, where chargeability is around 5.5 ms near the beginning of the line.

3.2. Geostatistical interpolation of geophysical data

The elevation of the interface from each of the electrical resistivity lines was georeferenced, interpolated with ordinary kriging (Priya and Dodagoudar, 2020), and contoured (Fig. 6). We used an isotropic spherical variogram model with a sill of 7 and range of 65 m. Cross validation revealed a very low RMS error between fitted and the inversion model-inferred elevations at 0.32 m. The interface elevation map shows a correlation with surface elevation as expected, where the northern bank is higher than the southern bank from Lines 1 through 7. It transitions to the opposite for the last three lines, where surface and interface elevation are higher. Along Line 4, however, a ridge appears that breaks an otherwise near continuous trough across the site. There are also obvious shortcomings in the data, evident by closed circles of low elevations in nearly all lines, suggesting that the lines should have been placed more closely together despite having a range greater than the mean line separation. Nevertheless, the existing dataset provides a good initial understanding of details of the interface.

The same geostatistical procedure was applied to the electrical resistivity and chargeability, using slices at constant depths (Fig. 7). At the shallowest depth, the electrical resistivity data show elongated conductive features that run along either side of the EFPC (Fig. 7a). In the middle depth, the elongated features are more isolated, but still elongated with direction of stream flow (Fig. 7b). At the deepest depth the elongated bodies are retained but weaker, and the influence of material below the interface at the center of the creek becomes apparent (Fig. 7c). We have observed bedrock in the stream itself and perhaps one of the largest downfalls of the methodology is not accounting for that in the upper slice. The model resolution of electrical resistivity decreases with depth, so targets become broader and larger in Fig. 7c.

The interpolated chargeability data shows a consistent pattern in all three slices (Figs. 7d-7f) with significantly higher values south of the stream below the stream curve. Upstream of the curve, the high chargeability values are on the north bank where the land elevation is lower than the south bank. The correlation length of the chargeability is also larger than that of the resistivity and continuity of high values are shown across the lines. The chargeability and resistivity data are not perfectly correlated suggesting different processes for each data set.

4. Discussion

4.1. Bedrock architecture

Examining all of the electrical resistivity lines, we believe the interface modeling is a good proxy for identifying the top of the bedrock. The

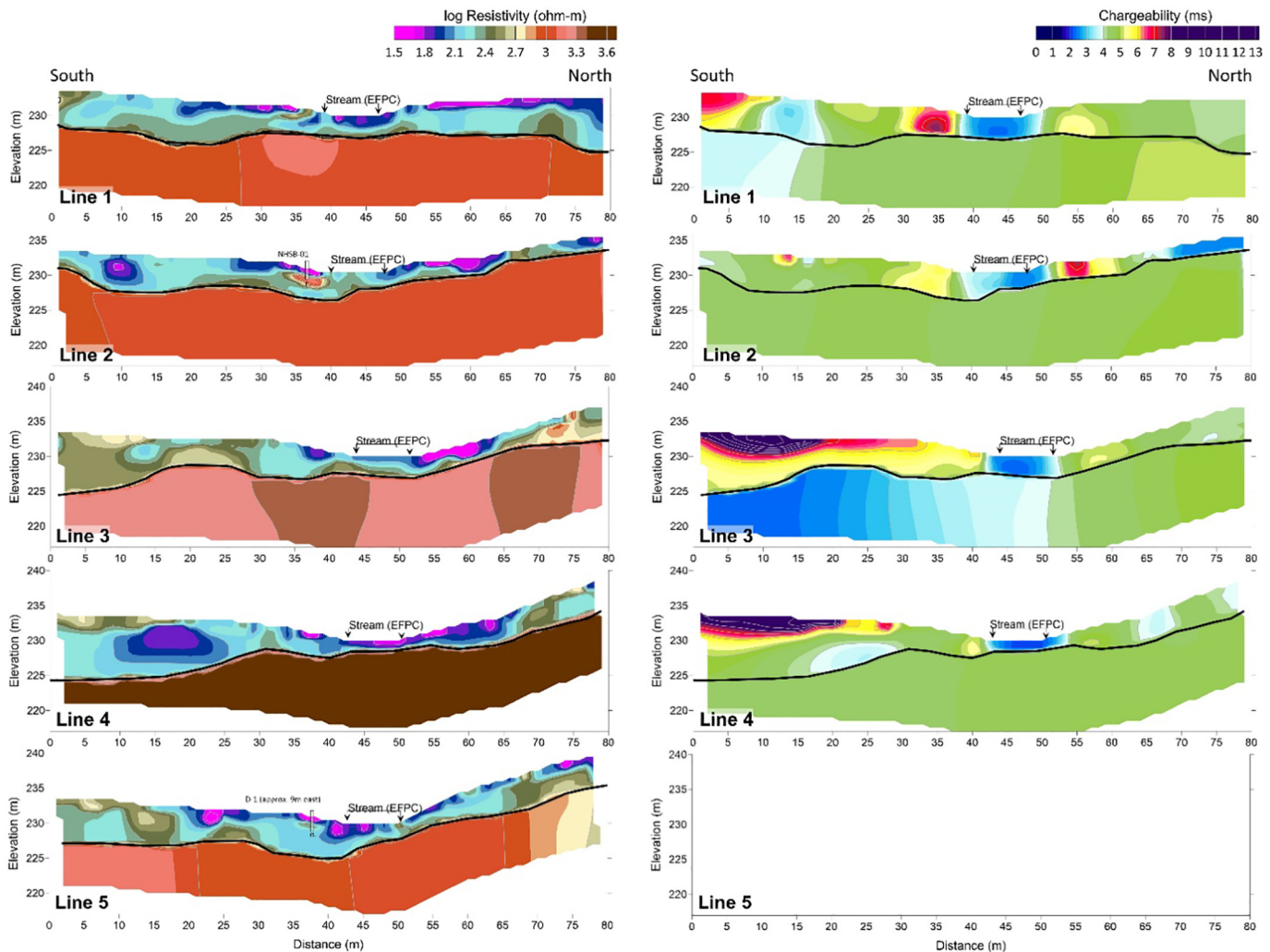


Fig. 4. Electrical resistivity and IP inversion results for Lines 1–5 along EFPC. The interface with lowest model RMS is displayed as a thick black line. Nearby boreholes and drilling data from Fig. 1 are also overlain on a few sections. The IP model for Line 5 is missing due to the excessive noise observed in the data.

best performing bedrock interface value using the KIM is represented by a thick black line in each of the line's inversion model. Throughout much of the survey lines, the bedrock interface correlates with the surface topography. Unfortunately, very little ancillary evidence exists for the accuracy of the interface, other than refusal depth in NHSB-01 through -04 which ranged in elevation from 229.5 m to 229.7 m and D-2 and D-3 with elevations of 229.7 m and 229.5 m, respectively. These data are shown for reference in Figs. 4 and 5. The open hole in D-1 had a completion elevation of 229 m (Fig. 1c). NHSB-01 and NHSB-02 are near Line 2 and the interface for this line at the borings is above 228 m, a difference of approximately one meter. The resistivity data shows a highly resistive feature that is roughly 3.8 m across and 0.9 m thick; the feature may be causing the refusal. Line 5 is close to D-1 and shows the interface to be around elevation 225 m, which is consistent with the lack of refusal during drilling. The modeled resistivity values for bedrock generally range from 2.9 to 3.1 in log scale resistivity. Line 4 showed much higher values of 3.4. It is unclear, without additional expensive bedrock drilling, if the variation in bedrock resistivity is a function of model variability or if the range of values are representations of a degree of fracturing or porosity in the limestone. In Fig. 5, Lines 6 through 10 also exhibit narrow bedrock values, with Line 7 having a vertical feature that could be interpreted as a fault, but doesn't carry through to any of the adjacent lines for validation.

Generally, the bedrock has been reported as having low porosity, but karst is possible (McMaster, 1963). The IP data for the bedrock shows

fairly low chargeability values with the exception of Line 9, where chargeability is around 5.5 ms near the beginning of the line. Low bedrock chargeability values with high resistivity values implies an absence of clay. If the limestone bedrock has appreciable porosity, fracturing, or karst, it is likely filled with water and not clay. Additional drilling would be needed to confirm this hypothesis.

The geostatistical interpolation of the bedrock interface reveals potential unique architecture that could contribute to the difficulty in explaining the Hg mass flux. The low bedrock elevation on the south bank of EFPC could trap Hg during very low flow periods or push the Hg inland during sudden stream surges if the hydraulic gradient reverses during initial high flows. Then, during the receding flows, the gaining reach of the stream could see a slow mass influx. This hypothesis would need to be validated with additional piezometers, high frequency monitoring, and detailed modeling, all of which are beyond the scope of this paper. However, the work here in identifying the bedrock interface would provide a reasonable starting point for model geometry.

4.2. Soil texture and hyporheic zone

Overlying the bedrock interface is a layer of soil reaching up to 6 to 8 m in thickness according to the geophysical results. The soil is thicker south of the stream bank in the floodplain compared to the north in Lines 1 through 7. Undulations in the interface along the south bank causes the soil to be much thicker above troughs. Two notable troughs

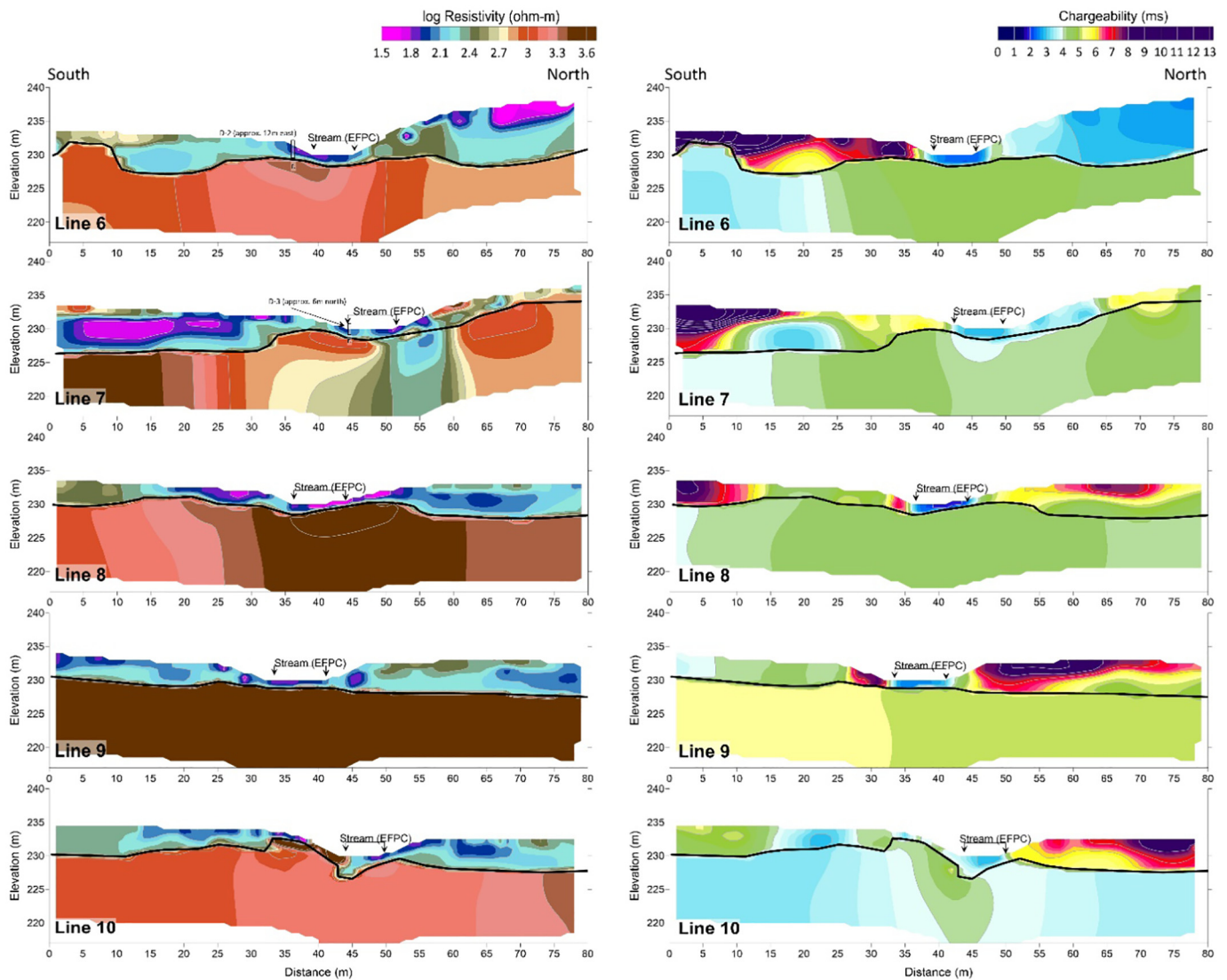


Fig. 5. Electrical resistivity and IP inversion results for Lines 6–10 along EFPC. The interface with lowest model RMS is displayed as a thick black line. Nearby boreholes and drilling data from Fig. 1 are also overlain on a few sections.

include one that is immediately south of the stream and another near the beginning of most of the lines. The variability in the bedrock interface and thickness of the overlying soil sediments illustrates the ubiquitous heterogeneity of the subsurface and the need for the development of subsurface characterization methods (e.g., Yeh et al., 2015).

The sediments are significantly more electrically conductive than the bedrock below. Chambers et al. (2014) showed slightly different results with conductive bedrock and resistive sediments based on the geological makeup of the material. The sediment descriptions for our site along EFPC mostly include loam, silty loam, silty clay loam, clay loam, and clay, which are mostly shown in the upper elevations. A few samples from NHSB-01 through NHSB-04 and D-3 list sands and gravels at lower elevations, with gravel percentage increasing with depth until refusal. The chargeability information is one discriminator of higher clay content and Lines 1, 3, and 4 all show high chargeability values on the order of 7 to 10 ms. The high chargeabilities are closer to the surface, but occasionally reach bedrock (e.g., Line 1 near the south stream bank). On the south bank of Line 7 is a point bar with shallow bedrock. The drilling that occurred at D-3 (Fig. 1c) discovered shallow sands and gravels before hitting refusal at around an elevation of 229.5 m. This is exactly where the resistivity model shows the interface to exist.

The stream itself is shown to be extremely low chargeability. Anecdotally, the creek bed has the appearance of being armored with gravel and cobbles on top and finer grained materials in the interstices and underlying the armored surface. There is also a lateral textural gradient across the channel with accumulation of fine grained materials at the channel margins and coarser materials near the thalweg. However, overall the unconsolidated materials are a relatively thin veneer over the bedrock in the creek channel proper.

One last observation is that the resistivity features in the lower two slices of Fig. 7b and c mildly resemble stream braiding, especially where the bedrock elevation was at its lowest. However, this is one of several possible interpretations that could include simply a unique depositional pattern or errors in the interpolation methodology. Additional data, including confirmatory drilling and analysis, with higher density geophysical surveys are needed to evaluate which of the interpretations may be more likely.

4.3. Influences of vegetation

Another interpretation of the IP results is that the organic carbon content may also be influencing the chargeability. There is a distinct change in dominant vegetation in the floodplain that spatially correlates

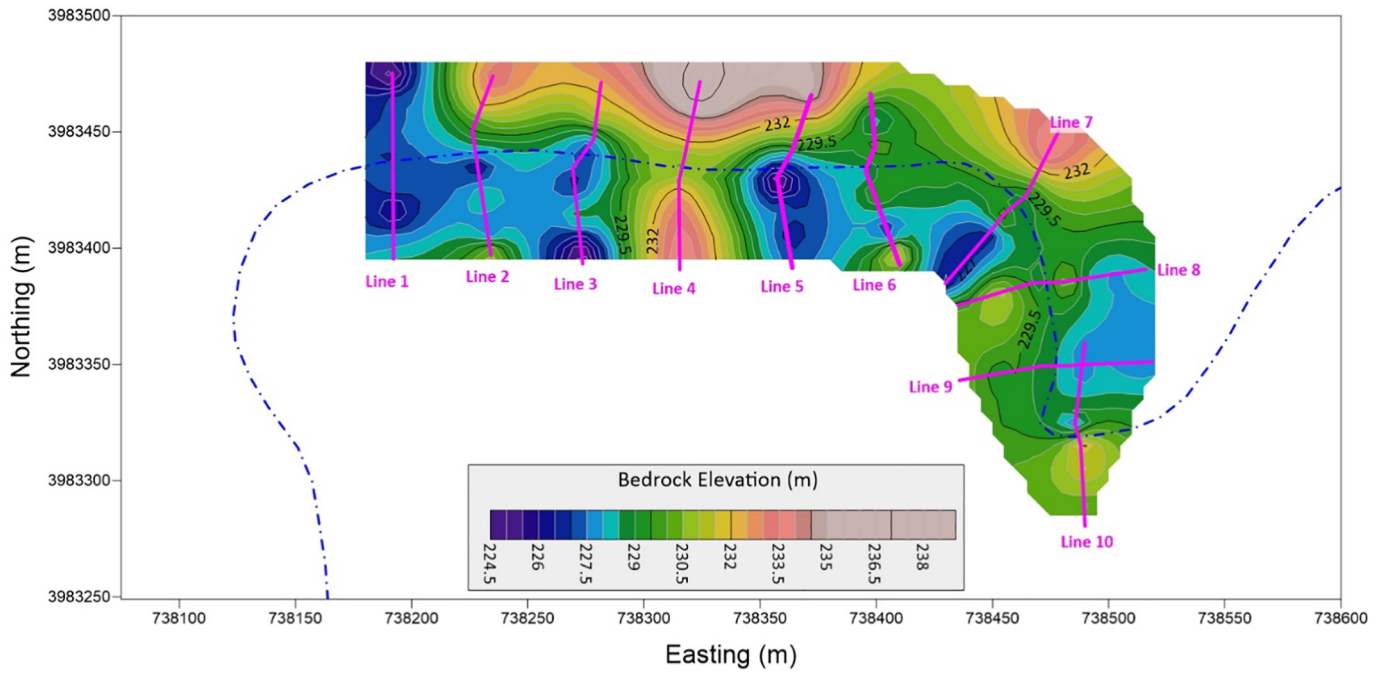


Fig. 6. Interpolated bedrock elevation from electrical resistivity profiles.

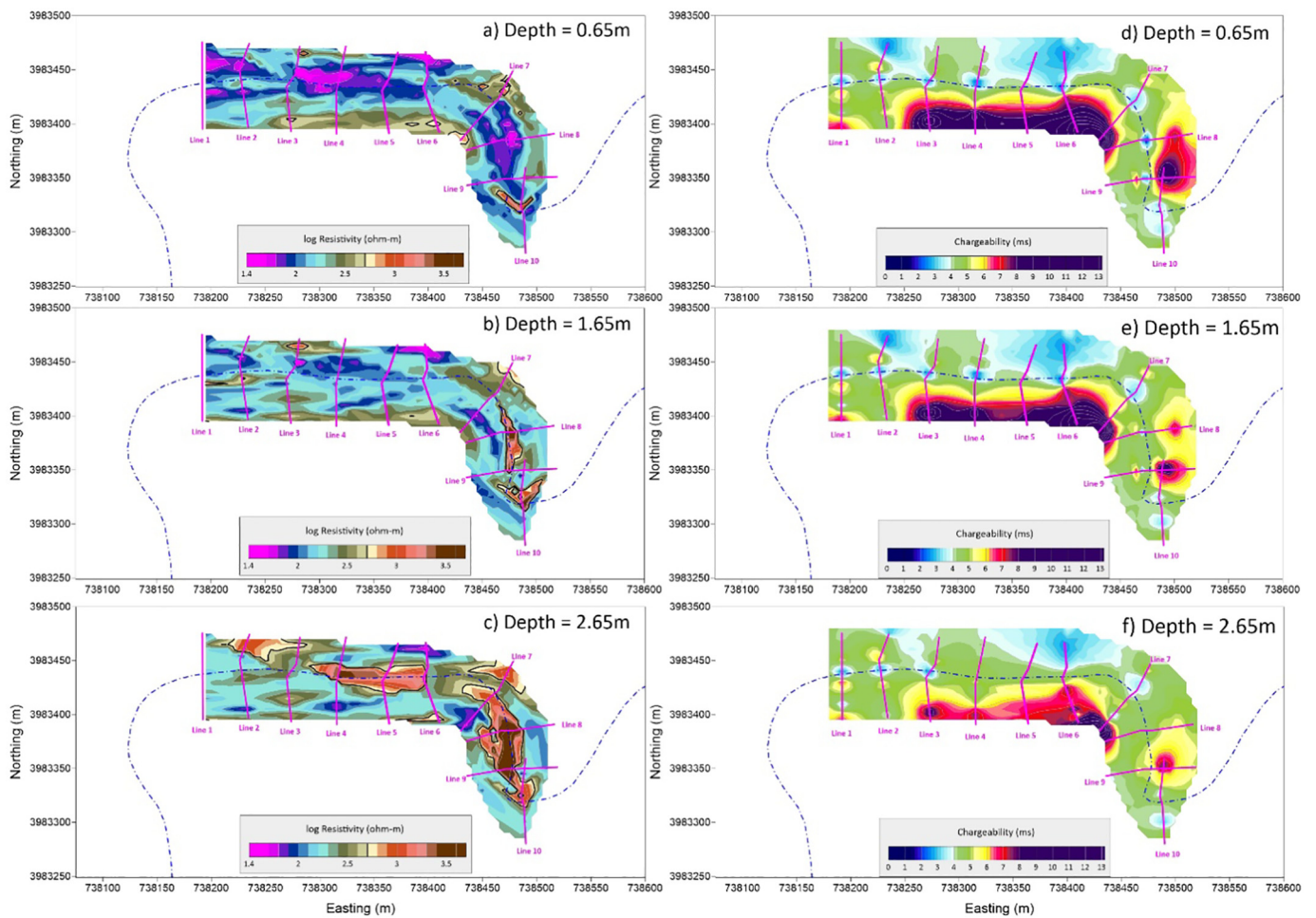


Fig. 7. Interpolated resistivity and chargeability data at three depths 0.65 m, 1.65 m, and 2.65 m: a)–c) resistivity; d)–f) chargeability.

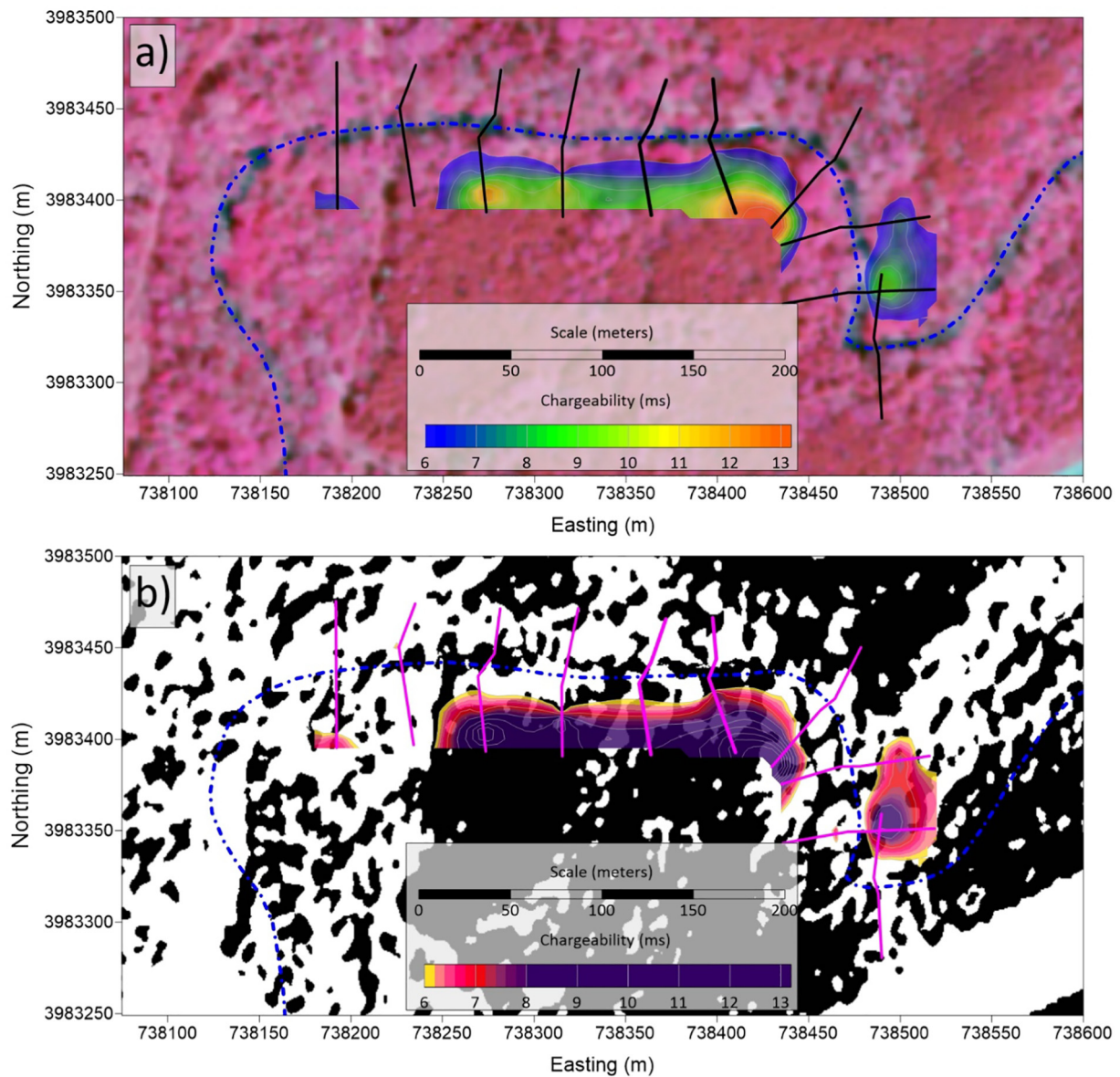


Fig. 8. Correlating vegetation differences with chargeability along EFPC with creek centerline and geophysical line locations highlighted: a) 2015 LiDAR data and 2014 USDA NAIP color infrared imagery; b) unsupervised image classification of the NAIP CIR imagery within the forest layer showing deciduous (white) and evergreen (black) forest.

with the high chargeability, from a dense evergreen stand with no understory to deciduous trees and an herbaceous understory. The work by Slater and Reeve (2002) on peatlands showed that the high surface charge and high cation exchange capacity of partially decomposed organic matter was more polarizable than the marine clays.

To further investigate the vegetation correlation between evergreen and deciduous forest, we first mapped all forest canopy using 2015 LiDAR data and 2014 USDA NAIP color infrared (CIR) imagery (Fig. 8a). We identified forest canopy by first generating a bare earth digital elevation model (DEM) using LiDAR ground returns and a first return digital surface model (DSM). DEM values were then subtracted from DSM values to identify areas where first returns were fifteen feet or greater from ground returns. Then we calculated the Normalized Difference Vegetation Index for the potential forest areas (i.e. areas where $(DSM - DEM) > 15'$) from the NAIP imagery to find areas of healthy vegetation and remove man-made structures from the forest layer. Finally, we ran an unsupervised image classification of the NAIP CIR imagery within the forest layer to distinguish between deciduous and evergreen forest (Fig. 8b). The series of contoured chargeability plots in Fig. 8 focused

on high values above 6 ms and have different color scales in order for the data to be easily visible with false color vegetation in the figures. These data show that there is a link between vegetation type and chargeability. Two hypotheses that could explain the correlation include: 1) the evergreen forest is providing a level of organic material to the soil that is directly causing increased chargeability; and 2) the evergreen forest prefers soils of high chargeability, as these soils are likely more clay rich. To validate either hypothesis, further investigation is needed.

5. Conclusions

The hyporheic zone and adjacent stream bank sediments along a short reach of the EFPC was investigated with electrical resistivity and IP to better understand bedrock architecture and soil texture. The data were collected along ten profiles spaced about 50 m apart and covered different aspects of the stream environment that included floodplains, banks, point bars, and variability in vegetation. A unique acquisition and modeling method was undertaken to synthesize the data into interpretable formats that included: 1) acquiring electrical data with an array

that has both high resolution and high signal to noise; 2) iterative bedrock picking workflow that minimized model errors; 3) interpolation of model information across the survey area that accommodated the unique geostatistical structure offered by the different datasets. The derivation of final model products were not necessarily efficiently produced, but their careful creation allowed for detailed analysis of features that would not necessarily been observed using other methodologies.

The general model behavior showed that for each profile, the bedrock was comprised of low conductivity, low chargeability material, with low variability. The soil above was higher in conductivity and chargeability and also highly variable. We were able to delineate the soil from bedrock using the known interface method, picking logarithmically transformed resistivity values that ranged from 2.4 to 3.0. The interface was then used in sharp boundary modeling to decouple the bedrock from the unconsolidated sediments. The elevation of the interface was shown to be somewhat correlated with the land surface but with undulations in the flood plain. The interpolated bedrock elevation map taken from georeferenced interface picks showed a nearly continuous trough running alongside the EFPC, except for a bedrock ridge in Line 4. The data from Line 4 seem out of place and perhaps speaks to the uncertainty in the method.

The electrical resistivity data above the interface, representing various textured soils at different degrees of saturation show small scale features that resemble a braided stream channel, although this interpretation is speculative. The braiding is correlated with floodplain location and the bedrock trough. The chargeability data, on the other hand, is comprised of large scale features, where the floodplain material is high, and low everywhere else including on the steeper slopes above the stream and in the stream itself. When chargeability is coupled with the resistivity, we may be seeing some variability of sandy clay or clayey sand based on slight changes in resistivity values. Alternatively, a vegetation classification between evergreen and deciduous forest could explain the chargeability observations. A larger view with more resistivity lines spread across larger parts of EFPC and deeper in the floodplain would help provide context to these findings and to understand if it is a larger pattern to help explain mass transport of mercury in an out of the hyporheic zone.

Credit author statement

Dale F. Rucker: Conceptualization, Methodology, Formal analysis, Visualization, Writing - original draft, Writing - review & editing.

Chia-Hsing Tsai: Methodology, Investigation, Resources, Data curation, Writing - original draft, Writing - review & editing.

Kenneth C. Carroll: Conceptualization, Methodology, Resources, Supervision, Project administration, Funding acquisition, Writing - original draft, Writing - review & editing.

Scott Brooks: Validation, Supervision, Project administration, Funding acquisition.

Eric M. Pierce: Supervision, Project administration, Funding acquisition.

April Ulery: Validation.

Christopher Derolph: Visualization.

Declaration of Competing Interest

The authors declare that they have no known competing financial interests or personal relationships that could have appeared to influence the work reported in this paper.

Acknowledgements

This work was primarily supported by the Department of Energy Minority Serving Institution Partnership Program (MSIPP) managed by the

Savannah River National Laboratory. A portion of this research was sponsored by the Office of Biological and Environmental Research within the Office of Science of the U.S. Department of Energy (DOE), as part of the Mercury Science Focus Area project at the Oak Ridge National Laboratory (ORNL). The DOE will provide public access to these results of federally sponsored research in accordance with the DOE Public Access Plan (<http://energy.gov/downloads/doe-public-access-plan>). ORNL is managed by UT-Battelle, LLC under Contract No. DE-AC05-00OR22725 with DOE. We appreciate the assistance of Kenneth Lowe, Michael Jones, Nikki Jones, Justin Milavec, Tanzila Ahmed, Chris Kubicki, and Amanda Lara.

References

- Anibas, C., Schneidewind, U., Vandersteen, G., Joris, I., Seuntjens, P., Batelaan, O., 2016. From streambed temperature measurements to spatial-temporal flux quantification: using the LPML method to study groundwater-surface water interaction. *Hydrol. Process.* 30 (2), 203–216.
- Benoit, S., Ghysels, G., Gommers, K., Hermans, T., Nguyen, F., Huysmans, M., 2019. Characterization of spatially variable riverbed hydraulic conductivity using electrical resistivity tomography and induced polarization. *Hydrogeol. J.* 27 (1), 395–407.
- Bianchin, M.S., Smith, L., Beckie, R.D., 2011. Defining the hyporheic zone in a large tidally influenced river. *J. Hydrol.* 406 (1–2), 16–29.
- Boano, F., Harvey, J.W., Marion, A., Packman, A.I., Revelli, R., Ridolfi, L., Wörman, A., 2014. Hyporheic flow and transport processes: mechanisms, models, and biogeochemical implications. *Rev. Geophys.* 52 (4), 603–679.
- Brooks, S.C., Southworth, G.R., 2011. History of mercury use and environmental contamination at the Oak Ridge Y-12. *Plant. Environ. Poll.* 159 (1), 219–228.
- Brooks, S., Eller, V., Dickson, J., Earles, J., Lowe, K., Mehlhorn, T., Olsen, T., DeRolph, C., Watson, D., Phillips, D., Peterson, M., 2017. Mercury Content of Sediments in East Fork Poplar Creek: Current Assessment and Past Trends. ORNL/TM-2016, 578. Tenn. Oak Ridge National Lab.
- Busato, L., Boaga, J., Perri, M.T., Majone, B., Bellin, A., Cassiani, G., 2019. Hydrogeophysical characterization and monitoring of the hyporheic and riparian zones: the Vermigliana Creek case study. *Sci. Total Environ.* 648, 1105–1120.
- Cardenas, M.B., Markowski, M.S., 2010. Geoelectrical imaging of hyporheic exchange and mixing of river water and groundwater in a large regulated river. *Environ. Sci. Technol.* 45 (4), 1407–1411.
- Chambers, J.E., Wilkinson, P.B., Penn, S., Meldrum, P.I., Kuras, O., Loke, M.H., Gunn, D.A., 2013. River terrace sand and gravel deposit reserve estimation using three-dimensional electrical resistivity tomography for bedrock surface detection. *J. Appl. Geophys.* 93, 25–32.
- Chambers, J.E., Wilkinson, P.B., Uhlemann, S., Sorensen, J.P.R., Roberts, C., Newell, A.J., Ward, W.O.C., Binley, A., Williams, P.J., Goody, D.C., Old, G., 2014. Derivation of lowland riparian wetland deposit architecture using geophysical image analysis and interface detection. *Water Resour. Res.* 50 (7), 5886–5905.
- Clémence, H., Marc, P., Véronique, D., Tohir, A., 2017. Monitoring an artificial tracer test within streambed sediments with time lapse underwater 3D ERT. *J. Appl. Geophys.* 139, 158–169.
- Crook, N., Binley, A., Knight, R., Robinson, D.A., Zarnetske, J., Haggerty, R., 2008. Electrical resistivity imaging of the architecture of streambed sediments. *Water Resour. Res.* 44 (4) W00D13.
- Cubbage, B., Noonan, G.E., Rucker, D.F., 2017. A modified Wenner array for efficient use of eight-channel resistivity meters. *Pure Appl. Geophys.* 174 (7), 2705–2718.
- Demers, J.D., Blum, J.D., Brooks, S.C., Donovan, P.M., Miller, C.L., Riscassi, A.L., Zheng, W., Gu, B., 2018. Hg isotopes reveal in-stream processing and legacy inputs in East Fork Poplar Creek, Oak Ridge, TN, USA. *Environ. Sci. Process. Impacts* 20 (4), 686–707.
- Dickson, J.O., Mayes, M., Earles, J.E., Mehlhorn, T.L., Lowe, K.A., Peterson, M.J., Pierce, E.M., 2015. Soil Investigation of Lower East Fork Poplar Creek (No. ORNL/TM-2015/374). Oak Ridge National Lab.(ORNL), Oak Ridge, TN.
- Dickson, J.O., Mayes, M.A., Brooks, S.C., Mehlhorn, T.L., Lowe, K.A., Earles, J.K., Goñez-Rodriguez, L., Watson, D.B., Peterson, M.J., 2019. Source relationships between streambank soils and streambed sediments in a mercury-contaminated stream. *J. Soils Sediments* 19 (4), 2007–2019.
- Dong, W.M., Liang, L.Y., Brooks, S., Southworth, G., Gu, B.H., 2010. Roles of dissolved organic matter in the speciation of mercury and methylmercury in a contaminated ecosystem in Oak Ridge, Tennessee. *Environ. Chem.* 7 (1), 94–102.
- Elwaseif, M., Slater, L., 2012. Improved resistivity imaging of targets with sharp boundaries using an iterative disconnect procedure. *J. Environ. Eng. Geophys.* 17 (2), 89–101.
- Florsch, N., Llubes, M., Téreygeol, F., Ghorbani, A., Roblet, P., 2011. Quantification of slag heap volumes and masses through the use of induced polarization: application to the Castel-Minier site. *J. Archaeol. Sci.* 38 (2), 438–451.
- Gaona, J., Meinikmann, K., Lewandowski, J., 2019. Identification of groundwater exfiltration, interflow discharge, and hyporheic exchange flows by fibre optic distributed temperature sensing supported by electromagnetic induction geophysics. *Hydrol. Process.* 33 (10), 1390–1402.
- Gilmour, C.C., Podar, M., Bullock, A.L., Graham, A.M., Brown, S.D., Somenahally, A.C., Johs, A., Hurt Jr., R.A., Bailey, K.L., Elias, D.A., 2013. Mercury methylation by novel microorganisms from new environments. *Environ. Sci. Technol.* 47 (20), 11810–11820.

- Hsu, H.L., Yanites, B.J., Chen, C.C., Chen, Y.G., 2010. Bedrock detection using 2D electrical resistivity imaging along the Peikang River, Central Taiwan. *Geomorphology* 114 (3), 406–414.
- Hsu, L., Finnegan, N.J., Brodsky, E.E., 2011. A seismic signature of river bedload transport during storm events. *Geophys. Res. Lett.* 38 (13).
- Johansson, S., Fiandaca, G., Dahlin, T., 2015. Influence of non-aqueous phase liquid configuration on induced polarization parameters: conceptual models applied to a time-domain field case study. *J. Appl. Geophys.* 123, 295–309.
- Johnson, T.C., Slater, L.D., Ntarlagiannis, D., Day-Lewis, F.D., Elwaseif, M., 2012. Monitoring groundwater–surface water interaction using time-series and time-frequency analysis of transient three-dimensional electrical resistivity changes. *Water Resour. Res.* 48 (7), W07506.
- Loar, J.M., Stewart, A.J., Smith, J.G., 2011. Twenty-five years of ecological recovery of East Fork Poplar Creek: review of environmental problems and remedial actions. *Environ. Manag.* 47 (6), 1010–1020.
- Loke, M.H., 2017. RES2DINV Software. *Geoelectrical Imaging 2D and 3D. Instruction manual.* Geotomo Software.
- Loke, M.H., Wilkinson, P.B., Chambers, J.E., 2010. Fast computation of optimized electrode arrays for 2D resistivity surveys. *Comput. Geosci.* 36 (11), 1414–1426.
- Loke, M.H., Chambers, J.E., Rucker, D.F., Kuras, O., Wilkinson, P.B., 2013. Recent developments in the direct-current geoelectrical imaging method. *J. Appl. Geophys.* 95, 135–156.
- Loke, M.H., Kuras, O., Chambers, J.E., Rucker, D.F., Wilkinson, P.B., 2020. Instrumentation, electrical resistivity. *Encyclopedia of Solid Earth Geophysics*, pp. 1–7.
- Magliozzi, C., Coro, G., Grabowski, R.C., Packman, A.I., Krause, S., 2019. A multiscale statistical method to identify potential areas of hyporheic exchange for river restoration planning. *Environ. Model. Softw.* 111, 311–323.
- Maurya, P.K., Balbarini, N., Møller, I., Rønne, V., Christiansen, A.V., Bjerg, P.L., Auken, E., Fiandaca, G., 2018. Subsurface imaging of water electrical conductivity, hydraulic permeability and lithology at contaminated sites by induced polarization. *Geophys. J. Int.* 213 (2), 770–785.
- McLachlan, P.J., Chambers, J.E., Uhlemann, S.S., Binley, A., 2017. Geophysical characterisation of the groundwater–surface water interface. *Adv. Water Resour.* 109, 302–319.
- McMaster, W.M., 1963. Geologic map of the Oak Ridge Reservation, Tennessee. ORNL-TM-713. Tenn. Oak Ridge National Lab.
- Mermillod-Blondin, F., Winiarski, T., Foulquier, A., Perrissin, A., Marmonier, P., 2015. Links between sediment structures and ecological processes in the hyporheic zone: ground-penetrating radar as a non-invasive tool to detect subsurface biologically active zones. *Ecohydrology* 8 (4), 626–641.
- Miller, R.B., Heeren, D.M., Fox, G.A., Halihan, T., Storm, D.E., Mittelstet, A.R., 2014. The hydraulic conductivity structure of gravel-dominated vadose zones within alluvial floodplains. *J. Hydrol.* 513, 229–240.
- Mwakanyamale, K., Slater, L., Binley, A., Ntarlagiannis, D., 2012. Lithologic imaging using complex conductivity: lessons learned from the Hanford 300 Area. *Geophysics* 77 (6), E397–E409.
- Nguyen, F., Garambois, S., Jongmans, D., Pirard, E., Loke, M.H., 2005. Image processing of 2D resistivity data for imaging faults. *J. Appl. Geophys.* 57 (4), 260–277.
- Nordsiek, S., Diamantopoulos, E., Hördt, A., Durner, W., 2016. Relationships between soil hydraulic parameters and induced polarization spectra. *Near Surf. Geophys.* 14 (1), 23–37.
- Ntarlagiannis, D., Robinson, J., Soupios, P., Slater, L., 2016. Field-scale electrical geophysics over an olive oil mill waste deposition site: evaluating the information content of resistivity versus induced polarization (IP) images for delineating the spatial extent of organic contamination. *J. Appl. Geophys.* 135, 418–426.
- Peterson, M.J., Brooks, S.C., Mathews, T.J., Mayes, M.A., Johs, A., McManamay, R., Watson, D.B., Muller, K., Goñez-Rodríguez, L., Derolph, C., Nair, S., 2018. Mercury Remediation Technology Development for Lower East Fork Poplar Creek—FY 2018 Update. ORNL/SPR-2018/912.
- Priya, B.D., Dodagoudar, G.R., 2020. Spatial variability of depth to weathered rock for Chennai using geostatistical kriging. *Applications of Geomatics in Civil Engineering.* Springer, Singapore, pp. 95–105.
- Pryshlak, T.T., Sawyer, A.H., Stonedahl, S.H., Soltanian, M.R., 2015. Multiscale hyporheic exchange through strongly heterogeneous sediments. *Water Resour. Res.* 51 (11), 9127–9140.
- Ren, J., Zhang, W., Yang, J., Zhou, Y., 2019. Using water temperature series and hydraulic heads to quantify hyporheic exchange in the riparian zone. *Hydrogeol. J.* 27 (4), 1419–1437.
- Roberts, L.G., 1963. Machine Perception of Three-Dimensional Solids. Doctoral dissertation. Massachusetts Institute of Technology, Cambridge MA.
- Roth, D.L., Brodsky, E.E., Finnegan, N.J., Rickenmann, D., Turowski, J.M., Badoux, A., 2016. Bed load sediment transport inferred from seismic signals near a river. *J. Geophys. Res. Earth Surf.* 121 (4), 725–747.
- Rucker, D., 2010. Moisture estimation within a mine heap: an application of cokriging with assay data and electrical resistivity. *Geophysics* 75 (1), B11–B23.
- Schmandt, B., Aster, R.C., Scherler, D., Tsai, V.C., Karlstrom, K., 2013. Multiple fluvial processes detected by riverside seismic and infrasound monitoring of a controlled flood in the Grand Canyon. *Geophys. Res. Lett.* 40 (18), 4858–4863.
- Sherman, T., Roche, K.R., Richter, D.H., Packman, A.I., Bolster, D., 2019. A Dual Domain stochastic lagrangian model for predicting transport in open channels with hyporheic exchange. *Adv. Water Resour.* 125, 57–67.
- Slater, L.D., Reeve, A., 2002. Investigating peatland stratigraphy and hydrogeology using integrated electrical geophysics. *Geophysics* 67 (2), 365–378.
- Steelman, C.M., Kennedy, C.S., Capes, D.C., Parker, B.L., 2017. Electrical resistivity dynamics beneath a fractured sedimentary bedrock riverbed in response to temperature and groundwater–surface water exchange. *Hydrol. Earth Syst. Sci.* 21 (6), 3105.
- Toran, L., Nyquist, J.E., Fang, A.C., Ryan, R.J., Rosenberry, D.O., 2013. Observing lingering hyporheic storage using electrical resistivity: variations around stream restoration structures, Crabby Creek, PA. *Hydrol. Process.* 27 (10), 1411–1425.
- Ward, A.S., Gooseff, M.N., Singha, K., 2010. Imaging hyporheic zone solute transport using electrical resistivity. *Hydrol. Process.* 24 (7), 948–953.
- Ward, A.S., Gooseff, M.N., Fitzgerald, M., Voltz, T.J., Singha, K., 2014. Spatially distributed characterization of hyporheic solute transport during baseflow recession in a headwater mountain stream using electrical geophysical imaging. *J. Hydrol.* 517, 362–377.
- Weller, A., Slater, L., Binley, A., Nordsiek, S., Xu, S., 2015. Permeability prediction based on induced polarization: Insights from measurements on sandstone and unconsolidated samples spanning a wide permeability range. *Geophysics* 80 (2), D161–D173.
- Yeh, T.C., Khaleel, R., Carroll, K.C., 2015. *Flow through Heterogeneous Geologic Media.* Cambridge University Press.